Charge separation in monolayer WSe2 by strain engineering

Zhuofa Chen^{1*}, Weijun Luo^{2*}, Liangbo Liang³, Xi Ling^{2,5}, Anna K. Swan^{1,4,5}†

¹Department of Electrical and Computer Engineering, Boston University, Boston MA 02215, USA.

²Department of Chemistry, Boston University, Boston, MA 02215, USA.

³Center for Nanophase Materials Sciences, Oak Ridge National Laboratory, Oak Ridge, TN 37831, USA.

⁴Department of Physics, Boston University, Boston, MA 02215, USA.

⁵Photonics Center, Boston University, Boston, MA 02215, USA.

*These authors contributed equally

[†]Address correspondence to: swan@bu.edu

Key words: 2D materials, transition metal dichalcogenides (TMDCs), strain engineering, electrostatic-gating, exciton funneling

Abstract

Strain-engineering of the transition-metal dichalcogenide (TMDC) band gaps makes TMDCs promising optoelectronic materials. Controlling the flow of optically generated quasiparticles is desirable, but optical excitation creates strongly bound excitons due to the low dielectric screening in 2D materials, and are not separable by an applied external field. However, a localized strain field reduces the bandgap and generates an energy-band gradient that funnels neutral excitons to the strain apex. It would be even more advantageous to mimic a diode's internal field, where both bands bend in the same direction separating electrons and holes. This can be achieved if the TMDC band structure lowers both the conduction band minimum as well as the valence band maximum during strain-induced band narrowing (Type-II band narrowing). In this work, we have performed density functional theory calculations to show that the WSe₂ electronic structure under biaxial strain has this property. To test the type of band bending experimentally, we have combined localized strain with electrostatic doping to follow the evolution of photoluminescence of excitons and positive and negative trions as a function of doping. Our experimental results demonstrate that negative trions accumulate, while positive trion emission is near zero, indicating that both conduction and valence bands are bent downwards in the strained area. Unstrained WSe₂ does not show such tendency. Hence, localized strain provides an opportunity to locally separate electrons and holes and manipulate light-matter interaction for applications in novel strained-engineered optoelectronics.

Introduction

Two-dimensional (2D) transition metal dichalcogenides (TMDCs)-MX₂ (M=Mo, W; X=S, Se, Te), such as MoS₂, WS₂, and WSe₂¹ exhibit fascinating excitonic physics due to the reduced dielectric screening and enhanced Coulomb interaction in atomic thin 2D lattice². The binding energy of excitonic complexes (excitons, trions etc) in these materials is more than an order of magnitude greater than in bulk semiconductors due to the strong Coulomb interaction, forming stable neutral excitons and charged excitons (trions) even at room temperature. Large binding energy and direct band gap property of these 2D TMDCs results in bright and efficient emission, paving the way for excitonic devices, e.g. light-emitting devices.

The electronic band structure of 2D TMDCs can be easily tuned by strain owning to the atomic thin nature and high elasticity of the material, offering good opportunities for straining engineering. Straining 2D TMDCs bends the band structure and generates bandgap gradient, leading to exciton funneling³ and trion drift⁴ to the lowest bandgap region. Much research has been devoted to straining 2D TMDCs and manipulating excitonic complexes using straingradient devices. This include static straining device, e.g. micro/nano pillars⁵, wrinkled substrate³, and dynamic straining device, e.g. piezoelectric actuators^{6,7}, atomic force microscopy tips^{4,8}, nanogap⁹. Local nonuniform strain from these strain-gradient devices changes the band structure and thus offers excitonic states manipulation. Local strain modifies the exciton-phonon coupling of TMDCs and leads to exciton energies variation and asymmetric profile of exciton^{10,11}. Moreover, local strain induces the exciton funneling in TMDCs (e.g. MoS₂¹² and WS₂¹³, WSe₂¹⁴), leading to strong PL enhancement. By combining local strain and electrostatic gating, more novel effects can also be studied in TMDC. For instance, adjusting the strain and bias the

TMDCs to charge neutrality can inhibit nonradiative exciton-exciton annihilation (EEA) and improve the quantum yield (QY) to unity¹⁵.

WSe₂ is one of the most frequently used TMDCs and has great potential for electronic engineering applications, e.g., field effect transistors¹⁶, sensors¹⁷. Monolayer WSe₂ is a great system for studying various excitonic complexes due to its high quantum yield¹⁵. Though much research work has been carried out on uniform straining engineering of WSe₂^{18,19}, local strain can physically move excitons and trions in WSe₂ towards or away from the strain apex⁹. Electrostatic gating is an easy and efficient way to introduce external charges (holes or electrons) and study the dynamic and conversion of excitonic complexes (dark trions²⁰, exciton to trion²¹, exciton to biexciton²², biexciton to charged biexciton²³, etc.). In this study, we combine local strain and electrostatic gating, which offers considerable opportunities to study to study exciton funneling and excitonic complexes conversion in WSe₂. In particular, we are interested in the type of band bending that the strain causes. If the band "pinch" together, it will collect quasiparticles and charge carriers which is interesting for studying high density phenomena such as crossover between an exciton gas and electron-hole liquid. If on the other hand, the bandgap decreases while both bands bend in the same direction, ("Type-II")²⁴, it will cause charge separation. Density functional theory (DFT) calculations of the electronic bands under different strain does not keep track of the relative band position as a function of strain. Typically, the top of the valence band is arbitrarily chosen as a fixed reference point. In this work, we use the vacuum level to determine the absolute movement of the bands. Both experimental evidence and DFT calculations point to WSe₂ as Type-II band-bending.

In this work, we study excitonic complexes in monolayer WSe₂ using micropillar static local strain and electrostatic gating, as shown in Fig 1 to elucidate the relative changes to the band

structure. We explore the radiative efficiency of exciton and trion in the photoluminescence (PL) of unstrained and locally strained WSe₂ under different bias conditions at low temperatures. We find that exciton and trion emission from unstrained and locally strained WSe₂ respond differently to gating. For the unstrained film, trion emission dominates both positive and negative bias. For the locally strained film, however, we see a large fraction of negative trions when introducing external electrons, but only a negligible fraction of positive trion emission when external holes are injected. This indicates that the local strain induced by micropillars bends down both the conduction band and valence band of WSe₂, i.e., Type II, resulting in the accumulation of electrons and removal of holes in the lowest bandgap region, indicated in the top panel of Figure 1. This provides an opportunity to locally separate electrons and holes and manipulate light-matter interaction for applications in novel strained-engineered optoelectronics.

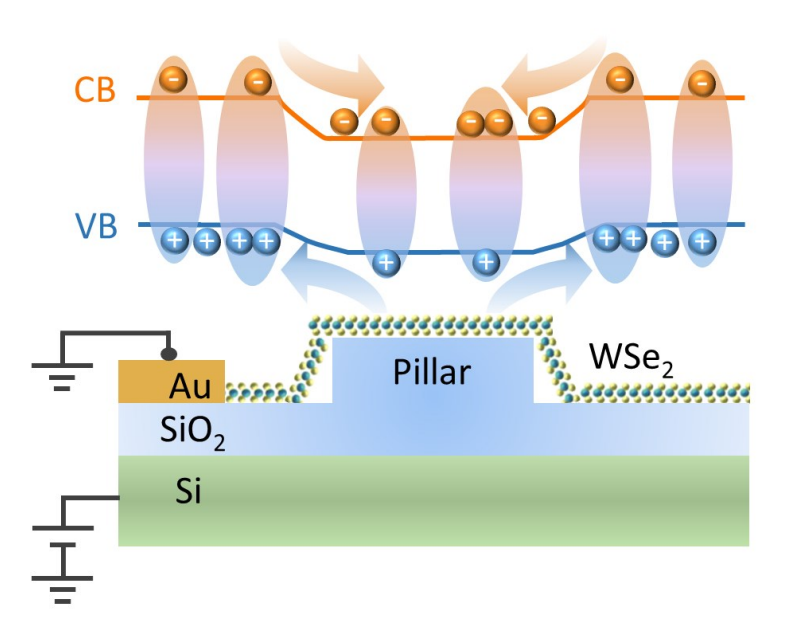


Figure 1 A schematic of the device for studying locally strained WSe₂ across micro-pillars. The upper panel shows the band diagram of WSe₂ over the micro-pillar and the direction of carrier movement. Excitons are funneled to the strained region and excess holes are repelled from the apex of the pillar.

The sample setup is illustrated in Figure 1. The WSe₂ film is connected to an electrode, which is grounded. The highly-doped Si provides the back gate on the WSe₂ sample and external electrons or holes can be introduced by positive or negative gate bias, respectively. The optical images and Atomic Force Microscopy images are shown in Figure S4. The localized strain on WSe₂ is generated by transferring a monolayer WSe₂ over micro-pillars (2 µm in diameter, 130 nm in height). The exciton PL peak shift corresponds to 0.26% using relative energy shift in strain-dependent PL spectra, 50 meV/% strain²⁵, shown in Figure S8. However, this strain is an underestimated value since the measured PL spectrum is convolutional results of the WSe2 sample within the laser spot. The local strain is estimated to be significantly higher since the generated strain is a combination of local height variations²⁶ and some degree of slipping^{3,27}, discussed below. The WSe₂ device is mounted onto a cryostage and pumped down to 10⁻⁶ Torr. The photoluminescence (PL) is measured using a continuous-wave (CW) laser with a wavelength of 532nm at a 77 K unless otherwise mentioned. Detailed sample preparation, device fabrication, and measurement setup are described in Supplementary information (SI), Figure S1-S5. The laser power is around ~140 nW, making sure that the excitation in the linear region is without thermal effect (Figure S6) and preventing the strain release due to high laser power. We found that the strain on the WSe₂ over a pillar would release if the laser power is higher than 1 μW, as shown in Figure S7.

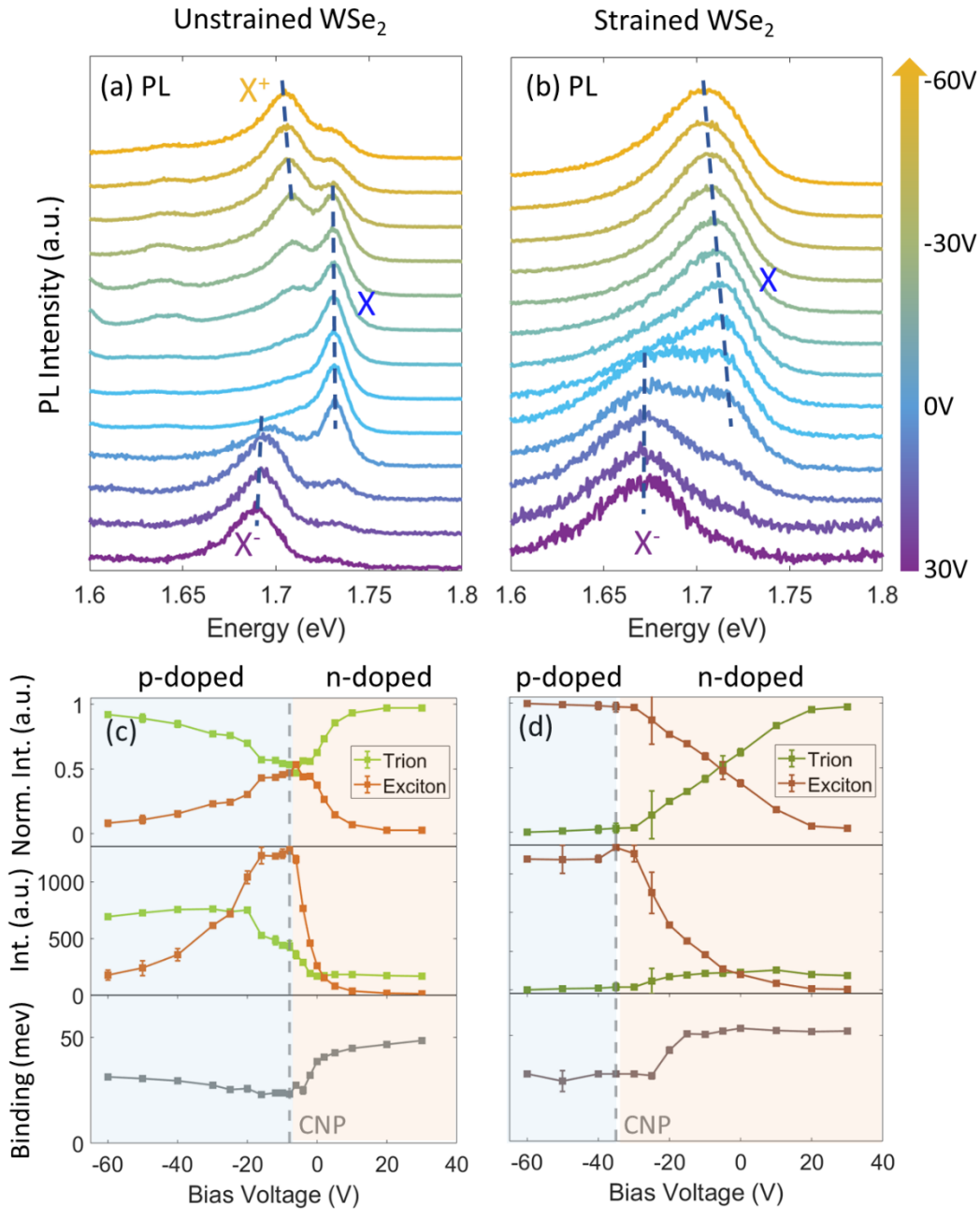


Figure 2 Photoluminescence under different gated voltages of unstrained and strained WSe₂. Waterfall plot of biased PL of unstrained WSe₂ (a) and strained WSe₂ (b). The exciton, positive trion, and negative trion are denoted as X, X+, and X-, respectively. The extracted normalized integrated intensity, intensity, and binding energy as a function of biased voltages of unstrained WSe₂ (c) and strained WSe₂ (d).

We first performed gated PL measurements on the unstrained WSe₂ layer on the substrate at 77 K. Figure 2a shows the evolution of PL of unstrained WSe₂ biased from 30V to -60V. The PL spectra show negative trion peaks at ~1.69 eV under positive gate bias, neutral exciton peaks at 1.73eV (E_{TB-} = 40 meV) with a charge neutrality point (CNP) at -8V, and positive trion peaks at ~1.705eV (E_{TB+} = 25 meV) under negative gate bias. Similar results are also reported previously^{20,22,23,28}. To analyze the data, the collected PL data is fitted using a combination of a Voigt profile (trion) and convoluted asymmetric long-tail profile (exciton), as shown in Figure S9. Figure 2c shows the fitted parameters under different bias voltages. The binding energy between trions and excitons is shown in the lower panel of Figure 2c. We see the positive trion has a lower binding energy than the negative trion as observed previously. This is due to the different short-range Coulomb exchange interactions between electrons and holes²¹. The middle panels of Figure 2c shows the extracted PL intensity of trion and exciton emission. The exciton emission achieves the maximum intensity at the CNP and vanishes under positive or negative bias where excitons are converted to trions²⁹. Positive and negative trion peaks emerge when the gate voltage is away from the CNP, and the intensity reaches a plateau at a doping level higher than $10^{12} \, \text{cm}^{-2}$ for the optical intensity used. Variation of normalized integrated intensity, peak intensity, and binding energy versus bias charge density is shown in Figure S10. The radiation efficiency of the trion peak depends on the quality of the WSe₂ sample. Both stronger negative trion peak intensity^{23,28,22,20,21} and stronger positive trion peak intensity^{30,31} in monolayer WSe₂ devices or BN encapsulated WSe₂ devices are reported previously. Here, we observe that the positive trions has higher intensity than negative trions. This might be because the positive trions have lower binding energy and are easier to thermalize. The location of CNP (-8V) indicates the mechanical exfoliated WSe₂ sample is originally n-doped due to the selenium vacancies³². Under positive bias, external electrons are introduced, and there are insufficient holes forming exciton and negative trion for radiative decay, so non-radiative decay such as Auger recombination dominates³³, causing lower quantum yield; On the other hand, doping hole into n-type semiconductor would favor recombination of radiative decay of many-body excitonic complexes³⁴ such as excitons and trions. We also observe that the positive trion intensity slowly decreases as negative bias increases because the higher doping levels favor the formation and recombination of positive dark trions³¹. Figure 2c upper panel plots the normalized integrated intensity exciton and trion, which shows the variation of trion and exciton in the radiative channel. Clearly, on both sides of the CNP, we observe PL that is dominated by the trion radiative decay channel, and decreasing exciton emission.

To experimentally determine the type of bandgap reduction, CB and VB pinching, or CB and VB both moving in the same direction (Type II), we carried out PL measurements of strained WSe₂ at a temperature of 77 K under different biased voltages. Figure 2b and d plot PL results at different biased voltages of WSe₂ strained using micropillars. We don't observe positive trions under negative bias, while we still see the negative trion peak under positive bias, as shown in the PL waterfall plot in Figure 2b. The extracted parameters, shown in Figure 2d, indicate exciton dominates the radiative channel even though holes are supplied. While under positive bias, we observe similar trion and exciton behavior as the plot from unstrained WSe₂ shown in Figure 2a and c. Hence, the local strain induced by the pillar changes the conduction band and valence band so that electrons can accumulate on the apex of the pillar while holes are repelled from the apex of the pillar (Figure 1, top). Under the positive bias, negative trions are formed similar to unstrained WSe₂ and dominate the radiative channel, shown in Figure 2d upper panel. Under negative bias, the exciton achieves 95% to 98 % emission ratio (exciton emission ratio is

defined as the integrated intensity of exciton over the integrated intensity of exciton and trion). This indicates that holes are repelled away from the pillar regime, and charge separation are realized in WSe₂ strained over a pillar. The extracted parameters discussed above versus charge doping levels are plotted in Figure S10b. We also performed similar experiments on WSe₂ strained using square pillars. The results show similar exciton and trion emission behavior as the WSe₂ strained using circle pillar (Figure S11). We still see strong exciton peak and weak positive trion peak under negative bias.

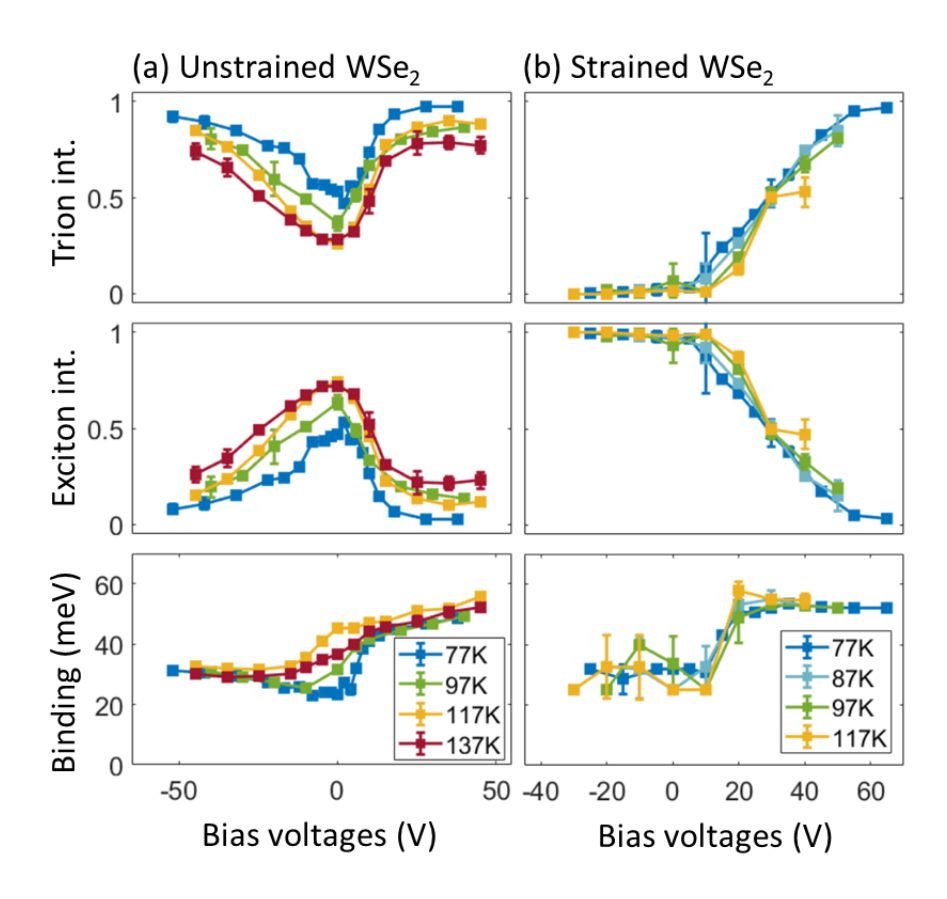


Figure 3 The extracted normalized integrated intensity (area ratio) of trion and exciton, the binding energy as a function of bias voltages of (a) unstrained WSe2 and (b) strained WSe₂ at different temperatures.

Increasing temperature delocalizes excitonic complexes and strengthens the non-radiative scattering (exciton phonon scattering) in WSe₂, leading to lower PL yield and suppression of trion PL^{35,36}. Thus temperature can also play an important role in the exciton-trion conversion mechanism strained WSe₂. We performed PL on unstrained and pillar-strained WSe₂ at different temperatures and biased voltages and studied the variation of the integrated intensity (area) of trion and exciton under different doping levels. Figure 3 shows the normalized trion and exciton integrated intensities, and the binding energies of unstrained and strained WSe2 at different temperatures from 77 K to 137 K. For unstrained WSe₂ shown in Figure 3a, the trion area decreases as the temperature increases; while the exciton area has the opposite behavior, the exciton area increases by ~25 % as temperature increases. This can be explained by the presence of dark excitons at low temperatures, and more dark states within the light cone are occupied at high temperature³⁷. Figure 3b shows similar plots of strained WSe₂. Firstly, the positive trion area is negligible, and the corresponding exciton area is dominant at all temperatures, indicating that the mechanism of holes flowing out of the happens under all the collected temperatures. However, on the electron doping side, we observed a decrease in the negative trion area and an increase of exciton as the temperature increases, similar to the results collected from unstrained WSe₂, shown in Figure 3a. The binding energy does not show a big difference at different temperatures except a shift in the CNP. The collected biased PL of unstrained and strained WSe₂ under different temperatures are shown in Figure S12. We only fit and analyze the PL spectra at the temperature up to 137 K since the trion and exciton peaks overlap too much at higher temperatures, and the fitting is unreliable.

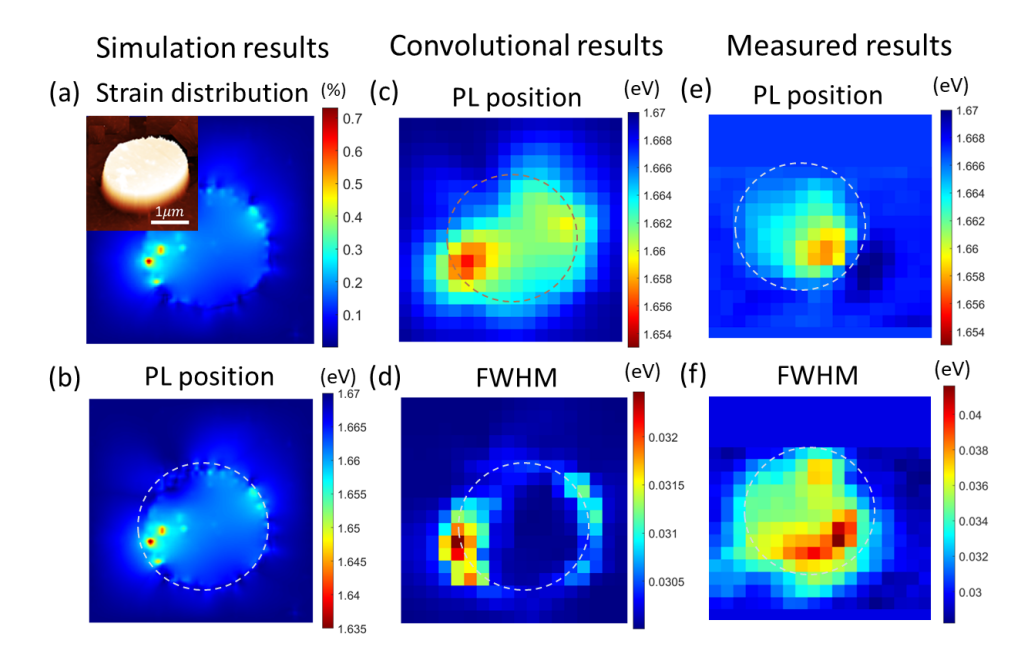


Figure 4 Simulated strain and PL distribution and measured PL. (a) Simulated biaxial tensile strain distribution of a circle pillar based on the AFM profile shown in inset, the scale bar is $1\mu m$. (b) The calculated PL position distribution based on the strain shown in (a). (c-d) The calculated convolutional PL position and PL FWHM of (b) using a laser spot size of 0.5 μm and a stride of 0.2 μm . (e-f) The experimental PL position and PL FWHM of a PL spatial mapping. The dashed circle indicates the location of the pillar.

We simulated the biaxial tensile strain distribution across different pillars via a finite element analysis (FEA) approach that calculates strain based on neighboring height differentials, reported by Darlington *et al.*²⁶ The FEA result of monolayer WSe₂ on a circle pillar (AFM image shown in Figure 4a inset) is shown in Figure 4a: the maximum strain always appears at the edges of the pillar and with a value of ~ 0.7 %. Figure 4b shows the distribution of PL peak position calculated from Figure 4a using a linear correlation between PL red-shift and tensile strain (50 meV / % strain)¹⁸. The strain simulation calculates local strain, while the measured samples strain over a region of WSe₂ within the laser spot, and averages the local strain variation. To compare calculated and measured strain mapping, we convolute the locals strain with the laser spot. The PL spectra at each pixel is generated using a Voigt profile with the same FWHM (20 meV) and a normalized amplitude. The convolutional process is performed by summing up the PL and dividing by the number of points within the laser spot diameter (0.5 μ m). The

convolutional result of PL energy and full width half maximum (FWHM) is shown in Figure 4(c-d). We can clearly see that the variation of PL peak position reduces by more than a factor of 2. Our measured data oversampled at 0.2 µm step size from a similar pillar, Figure 4 (e) and (f), show very good qualitative agreement with the calculated convolution. Hence we deduce that the actual local strain is larger than the measured 0.26 %.

Moreover, we performed first-principles DFT calculations of the electronic band structures of 1L WSe₂ under different amounts of biaxial tensile strains. As shown in Figure 5a, with the increasing strain, the calculated band gap decreases, corresponding to the red-shift of the A exciton; the decreasing rate is ~ -0.085 eV/% (as shown in Figure S13 (a)) that agrees with previous theoretical results³⁸. Note that experimental results have a smaller decreasing rate³⁸. Moreover, to understand the influences of increasing biaxial tensile strains on the positions of the energy bands, we re-align the energy bands with respect to the calculated vacuum energies (as shown in Figure S13 (b)). As shown in Figure 5a, with increasing biaxial tensile strain, both CBM and VBM downshift; Figure 5b shows that CBM downshifts with a larger rate of -0.112 eV / % compared to -0.028 eV % of VBM, corresponding to the Type-II band bending.²⁴ The larger band bending of the conduction band rather than that of the valence band suggests the accumulation of electrons and removal of holes in the lowest bandgap region. Hence, increasing strain in a Type II band bending aid holes to diffuse/drift away from the strain apex. The simulation results also support the experimental data that stronger exciton emission and weak positive trion PL are observed at CNP and hole doping conditions.

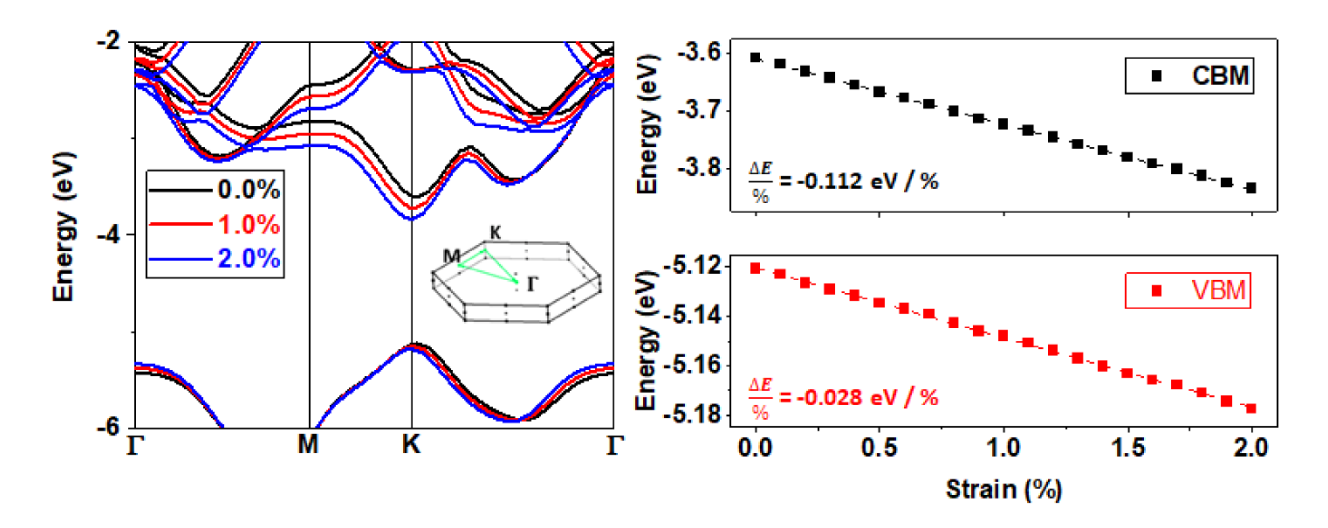


Figure 5 DFT simulations of monolayer (1L) WSe₂. (a) Band structures of 1L WSe₂ under 0%, 1.0% and 2.0% biaxial tensile strains, where the inset picture shows the selected high symmetry points along the first Brillouin zone. All band energies are aligned to the vacuum potential for direct comparison. (b) Red-shift rates of CBM and VBM from 0% to 2.0% biaxial tensile strains with an increment of 0.1%.

Conclusion

In conclusion, we performed experimental and theoretical analysis on biaxial strained monolayer WSe₂. We found that biaxial strain induced by micropillars bends down the conduction band and valence band of WSe₂, resulting in accumulating of electrons and dissipation of holes in the lowest bandgap region and leading to strong exciton emission (95 to 98 % of area ratio) and negligible positive trion at positive bias. The effect of temperature on the exciton and trion emission efficiency is also studied, and strong exciton emission with negligible positive trion are also observed at different temperatures. Finite element analysis of strain distribution and density functional theory calculations of band structures of WSe₂ agree well with the experimental results. This provides an opportunity to locally separate electrons and holes and manipulates light-matter interaction for applications in novel strained-engineered optoelectronics.

Methods

Device fabrication and measurement: Monolayer WSe₂ was obtained by the use of gold-mediated mechanical exfoliation³⁹; the detailed exfoliation process is shown in the supplementary information (SI). The WSe₂ device is fabricated by transferring WSe₂ over micropillars (2×2 um) grown by patterning and depositing 130 nm SiO₂ on the substrate (285nm SiO₂/Si⁺). The ground electrode (Au/Cr) is deposited next to the pillar array on the substrate by the use of a CHA electron-beam evaporator, and the gate electrode is formed by etching through

the SiO₂ layer and deposited Au/Cr films. The exfoliated WSe₂ monolayer flake is picked up using the water release method with PPC and transferred onto the pillar array, and connected with the ground electrode. The PPC is then removed using a critical point drier (CPD) with acetone to prevent the effect of surface tension on the WSe₂ during the evaporation of acetone. The photoluminescence (PL) is measured in a Cryo Industries cryostat using a continuous-wave laser (power: \sim 140nW, wavelength: λ = 532nm) and a 50× objective (spot size: 2.5um) on a Horiba T64000 spectrometer. More detailed fabrication process and measurement setup are described in Figures S1 and S2.

DFT simulations: Plane-wave DFT calculations were carried out using the Vienna Ab initio Simulation Package⁴⁰ (VASP) with projector augmented wave (PAW) pseudopotentials⁴⁰⁻⁴² for electron-ion interactions, , and the generalized gradient approximation (GGA) functional of Perdew, Burke and Ernzerhof⁴² (PBE) for exchange-correlation interactions. A unit cell of strain-free monolayer WSe₂ was modeled by creating a periodic slab with a vacuum separation of more than 22 Å to avoid the interactions with periodic images in the out-of-plane direction (Z direction). Both the lattice constants and atomic positions were optimized with a cutoff energy of 400 eV and 15×15×1 k-point samplings until the maximum force allowed on each atom was less than 0.001 eV / Å. The total volume of the structure was fixed during geometry optimization to avoid the structural collapse of the 2D slabs with vacuum separations. After the structural opmization, biaxial-strained monolayer WSe₂ structures were built, and their atomic positions were relaxed using the same parameter setting for strain-free monolayer WSe₂. The post-analysis of electronic band structures was carried out by using VASPKIT package.⁴³

Strain simulation: The strain simulation from the measured AFM profiles follows the analytical methods and codes developed by Darlington et al.²⁶ The AFM profiles of monolayer WSe₂ lying

on the different pillars were acquired by using a Veeco Dimension 3000 atomic force microscope (AFM).

Supporting information:

Detailed descriptions of the sample preparation, device fabrication, power- and temperaturedependent PL characterizations and detailed DFT simulation results of strain-dependent band gaps and vacuum energies.

Acknowledgement

This material is based upon work supported by the National Science Foundation (NSF) under Grant No. (1945364). W. L. and X.L. acknowledge the financial support from Boston University. X.L. acknowledges the membership of the Boston University Photonics Center. Theoretical modeling research was supported by the Center for Nanophase Materials Sciences (CNMS), which is a US Department of Energy, Office of Science User Facility at Oak Ridge National Laboratory. W.L. also acknowledges the high-performance computing resources of the Boston University Shared Computing Cluster (SCC).

References:

- (1) McDonnell, S. J.; Wallace, R. M. Atomically-Thin Layered Films for Device Applications Based upon 2D TMDC Materials. *Thin Solid Films* **2016**, *616*, 482–501. https://doi.org/10.1016/j.tsf.2016.08.068.
- (2) Raja, A.; Chaves, A.; Yu, J.; Arefe, G.; Hill, H. M.; Rigosi, A. F.; Berkelbach, T. C.; Nagler, P.; Schüller, C.; Korn, T.; Nuckolls, C.; Hone, J.; Brus, L. E.; Heinz, T. F.; Reichman, D. R.; Chernikov, A. Coulomb Engineering of the Bandgap and Excitons in Two-Dimensional Materials. *Nat Commun* **2017**, *8* (1), 15251. https://doi.org/10.1038/ncomms15251.
- (3) Castellanos-Gomez, A.; Roldán, R.; Cappelluti, E.; Buscema, M.; Guinea, F.; van der Zant, H. S. J.; Steele, G. A. Local Strain Engineering in Atomically Thin MoS ₂. *Nano Lett.* **2013**, *13* (11), 5361–5366. https://doi.org/10.1021/nl402875m.
- (4) Harats, M. G.; Kirchhof, J.; Qiao, M.; Greben, K.; Bolotin, K. Dynamics and Efficient Conversion of Excitons to Trions in Non-Uniformly Strained Monolayer WS2. 2020 Conference on Lasers and Electro-Optics (CLEO) 2020. https://doi.org/10.1038/s41566-019-0581-5.
- (5) Vutukuru, M.; Ardekani, H.; Chen, Z.; Wilmington, R. L.; Gundogdu, K.; Swan, A. K. Enhanced Dielectric Screening and Photoluminescence from Nanopillar-Strained MoS ₂ Nanosheets: Implications for Strain Funneling in Optoelectronic Applications. *ACS Appl. Nano Mater.* **2021**, *4* (8), 8101–8107. https://doi.org/10.1021/acsanm.1c01368.
- (6) Martín-Sánchez, J.; Trotta, R.; Mariscal, A.; Serna, R.; Piredda, G.; Stroj, S.; Edlinger, J.; Schimpf, C.; Aberl, J.; Lettner, T.; Wildmann, J.; Huang, H.; Yuan, X.; Ziss, D.; Stangl, J.; Rastelli, A. Strain-Tuning of the Optical Properties of Semiconductor Nanomaterials by Integration onto Piezoelectric Actuators. *Semicond. Sci. Technol.* 2017, 33 (1), 013001. https://doi.org/10.1088/1361-6641/aa9b53.
- (7) Hui, Y. Y.; Liu, X.; Jie, W.; Chan, N. Y.; Hao, J.; Hsu, Y.-T.; Li, L.-J.; Guo, W.; Lau, S. P. Exceptional Tunability of Band Energy in a Compressively Strained Trilayer MoS2 Sheet. *ACS Nano* **2013**, *7* (8), 7126–7131. https://doi.org/10.1021/nn4024834.
- (8) Moon, H.; Grosso, G.; Chakraborty, C.; Peng, C.; Taniguchi, T.; Watanabe, K.; Englund, D. Dynamic Exciton Funneling by Local Strain Control in a Monolayer Semiconductor. *Nano Lett.* **2020**, *20* (9), 6791–6797. https://doi.org/10.1021/acs.nanolett.0c02757.
- (9) Lee, H.; Koo, Y.; Choi, J.; Kumar, S.; Lee, H.-T.; Ji, G.; Choi, S. H.; Kang, M.; Kim, K. K.; Park, H.-R.; Choo, H.; Park, K.-D. Drift-Dominant Exciton Funneling and Trion Conversion in 2D Semiconductors on the Nanogap. *Sci. Adv.* **2022**, *8* (5), eabm5236. https://doi.org/10.1126/sciadv.abm5236.
- (10) Christiansen, D.; Selig, M.; Berghäuser, G.; Schmidt, R.; Niehues, I.; Schneider, R.; Arora, A.; de Vasconcellos, S. M.; Bratschitsch, R.; Malic, E.; Knorr, A. Phonon Sidebands in Monolayer Transition Metal Dichalcogenides. *Phys. Rev. Lett.* **2017**, *119* (18), 187402. https://doi.org/10.1103/PhysRevLett.119.187402.
- (11) Khatibi, Z.; Feierabend, M.; Selig, M.; Brem, S.; Linderälv, C.; Erhart, P.; Malic, E. Impact of Strain on the Excitonic Linewidth in Transition Metal Dichalcogenides. *2D Mater.* **2018**, 6 (1), 015015. https://doi.org/10.1088/2053-1583/aae953.
- (12) Mangu, V. S.; Zamiri, M.; Brueck, S. R. J.; Cavallo, F. Strain Engineering, Efficient Excitonic Photoluminescence, and Exciton Funnelling in Unmodified MoS2 Nanosheets. *Nanoscale* **2017**, *9* (43), 16602–16606. https://doi.org/10.1039/C7NR03537C.

- (13) Harats, M. G.; Kirchhof, J. N.; Qiao, M.; Greben, K.; Bolotin, K. I. Dynamics and Efficient Conversion of Excitons to Trions in Non-Uniformly Strained Monolayer WS2. *Nat. Photonics* **2020**, *14* (5), 324–329. https://doi.org/10.1038/s41566-019-0581-5.
- (14) So, J.-P.; Jeong, K.-Y.; Lee, J. M.; Kim, K.-H.; Lee, S.-J.; Huh, W.; Kim, H.-R.; Choi, J.-H.; Kim, J. M.; Kim, Y. S.; Lee, C.-H.; Nam, S.; Park, H.-G. Polarization Control of Deterministic Single-Photon Emitters in Monolayer WSe 2. *Nano Lett.* **2021**, *21* (3), 1546–1554. https://doi.org/10.1021/acs.nanolett.1c00078.
- (15) Kim, H.; Uddin, S. Z.; Higashitarumizu, N.; Rabani, E.; Javey, A. Inhibited Nonradiative Decay at All Exciton Densities in Monolayer Semiconductors. *Science* **2021**, *373* (6553), 448–452. https://doi.org/10.1126/science.abi9193.
- (16) Pudasaini, P. R.; Oyedele, A.; Zhang, C.; Stanford, M. G.; Cross, N.; Wong, A. T.; Hoffman, A. N.; Xiao, K.; Duscher, G.; Mandrus, D. G.; Ward, T. Z.; Rack, P. D. High-Performance Multilayer WSe2 Field-Effect Transistors with Carrier Type Control. *Nano Res.* **2018**, *11* (2), 722–730. https://doi.org/10.1007/s12274-017-1681-5.
- (17) Zhou, C.; Raju, S.; Li, B.; Chan, M.; Chai, Y.; Yang, C. Y. Self-Driven Metal—Semiconductor—Metal WSe2 Photodetector with Asymmetric Contact Geometries. *Advanced Functional Materials* **2018**, *28* (45), 1802954. https://doi.org/10.1002/adfm.201802954.
- (18) Carrascoso, F.; Li, H.; Frisenda, R.; Castellanos-Gomez, A. Strain Engineering in Single-, Bi- and Tri-Layer MoS2, MoSe2, WS2 and WSe2. *Nano Res.* **2021**, *14* (6), 1698–1703. https://doi.org/10.1007/s12274-020-2918-2.
- (19) Parto, K.; Azzam, S. I.; Banerjee, K.; Moody, G. Defect and Strain Engineering of Monolayer WSe2 Enables Site-Controlled Single-Photon Emission up to 150 K. *Nat Commun* **2021**, *12* (1), 3585. https://doi.org/10.1038/s41467-021-23709-5.
- (20) Liu, E.; van Baren, J.; Lu, Z.; Altaiary, M. M.; Taniguchi, T.; Watanabe, K.; Smirnov, D.; Lui, C. H. Gate Tunable Dark Trions in Monolayer \${\mathrm{WSe}}_{2}\$. *Phys. Rev. Lett.* **2019**, *123* (2), 027401. https://doi.org/10.1103/PhysRevLett.123.027401.
- (21) Courtade, E.; Semina, M.; Manca, M.; Glazov, M. M.; Robert, C.; Cadiz, F.; Wang, G.; Taniguchi, T.; Watanabe, K.; Pierre, M.; Escoffier, W.; Ivchenko, E. L.; Renucci, P.; Marie, X.; Amand, T.; Urbaszek, B. Charged Excitons in Monolayer WSe2: Experiment and Theory. *Phys. Rev. B* **2017**, *96* (8), 085302. https://doi.org/10.1103/PhysRevB.96.085302.
- (22) Li, Z.; Wang, T.; Lu, Z.; Jin, C.; Chen, Y.; Meng, Y.; Lian, Z.; Taniguchi, T.; Watanabe, K.; Zhang, S.; Smirnov, D.; Shi, S.-F. Revealing the Biexciton and Trion-Exciton Complexes in BN Encapsulated WSe2. *Nat Commun* **2018**, *9* (1), 3719. https://doi.org/10.1038/s41467-018-05863-5.
- (23) Ye, Z.; Waldecker, L.; Ma, E. Y.; Rhodes, D.; Antony, A.; Kim, B.; Zhang, X.-X.; Deng, M.; Jiang, Y.; Lu, Z.; Smirnov, D.; Watanabe, K.; Taniguchi, T.; Hone, J.; Heinz, T. F. Efficient Generation of Neutral and Charged Biexcitons in Encapsulated WSe2 Monolayers. *Nat Commun* **2018**, *9* (1), 3718. https://doi.org/10.1038/s41467-018-05917-8.
- (24) Feng, J.; Qian, X.; Huang, C.-W.; Li, J. Strain-Engineered Artificial Atom as a Broad-Spectrum Solar Energy Funnel. *Nature Photon* **2012**, *6* (12), 866–872. https://doi.org/10.1038/nphoton.2012.285.
- (25) Desai, S. B.; Seol, G.; Kang, J. S.; Fang, H.; Battaglia, C.; Kapadia, R.; Ager, J. W.; Guo, J.; Javey, A. Strain-Induced Indirect to Direct Bandgap Transition in Multilayer WSe 2. *Nano Lett.* **2014**, *14* (8), 4592–4597. https://doi.org/10.1021/nl501638a.

- (26) Darlington, T. P.; Krayev, A.; Venkatesh, V.; Saxena, R.; Kysar, J. W.; Borys, N. J.; Jariwala, D.; Schuck, P. J. Facile and Quantitative Estimation of Strain in Nanobubbles with Arbitrary Symmetry in 2D Semiconductors Verified Using Hyperspectral Nano-Optical Imaging. *The Journal of Chemical Physics* **2020**, *153* (2), 024702.
- (27) Rice, C.; Young, R. J.; Zan, R.; Bangert, U.; Wolverson, D.; Georgiou, T.; Jalil, R.; Novoselov, K. S. Raman-Scattering Measurements and First-Principles Calculations of Strain-Induced Phonon Shifts in Monolayer MoS 2. *Phys. Rev. B* **2013**, *87* (8), 081307. https://doi.org/10.1103/PhysRevB.87.081307.
- (28) Jones, A. M.; Yu, H.; Ghimire, N. J.; Wu, S.; Aivazian, G.; Ross, J. S.; Zhao, B.; Yan, J.; Mandrus, D. G.; Xiao, D.; Yao, W.; Xu, X. Optical Generation of Excitonic Valley Coherence in Monolayer WSe 2. *Nature nanotechnology* **2013**, *8* (9), 634–638. https://doi.org/10.1038/nnano.2013.151.
- (29) Lien, D.-H.; Uddin, S. Z.; Yeh, M.; Amani, M.; Kim, H.; Ager, J. W.; Yablonovitch, E.; Javey, A. Electrical Suppression of All Nonradiative Recombination Pathways in Monolayer Semiconductors. *Science* **2019**, *364* (6439), 468–471. https://doi.org/10.1126/science.aaw8053.
- (30) Van Tuan, D.; Scharf, B.; Wang, Z.; Shan, J.; Mak, K. F.; Žutić, I.; Dery, H. Probing Many-Body Interactions in Monolayer Transition-Metal Dichalcogenides. *Phys. Rev. B* **2019**, *99* (8), 085301. https://doi.org/10.1103/PhysRevB.99.085301.
- (31) Borghardt, S.; Kardynał, B. E.; Tu, J.-S.; Taniguchi, T.; Watanabe, K. Interplay of Excitonic Complexes in p -Doped WSe 2 Monolayers. *Phys. Rev. B* **2020**, *101* (16), 161402. https://doi.org/10.1103/PhysRevB.101.161402.
- (32) Hoffman, A. N.; Stanford, M. G.; Zhang, C.; Ivanov, I. N.; Oyedele, A. D.; Sales, M. G.; McDonnell, S. J.; Koehler, M. R.; Mandrus, D. G.; Liang, L.; Sumpter, B. G.; Xiao, K.; Rack, P. D. Atmospheric and Long-Term Aging Effects on the Electrical Properties of Variable Thickness WSe ₂ Transistors. *ACS Appl. Mater. Interfaces* **2018**, *10* (42), 36540–36548. https://doi.org/10.1021/acsami.8b12545.
- (33) Danovich, M.; Zólyomi, V.; Fal'ko, V. I.; Aleiner, I. L. Auger Recombination of Dark Excitons in WS 2 and WSe 2 Monolayers. *2D Mater.* **2016**, *3* (3), 035011. https://doi.org/10.1088/2053-1583/3/3/035011.
- (34) Pei, J.; Yang, J.; Yildirim, T.; Zhang, H.; Lu, Y. Many-Body Complexes in 2D Semiconductors. *Advanced Materials* **2019**, *31* (2), 1706945. https://doi.org/10.1002/adma.201706945.
- (35) Godde, T.; Schmidt, D.; Schmutzler, J.; Aßmann, M.; Debus, J.; Withers, F.; Alexeev, E. M.; Del Pozo-Zamudio, O.; Skrypka, O. V.; Novoselov, K. S.; Bayer, M.; Tartakovskii, A. I. Exciton and Trion Dynamics in Atomically Thin MoSe2 and WSe2: Effect of Localization. *Phys. Rev. B* **2016**, *94* (16), 165301. https://doi.org/10.1103/PhysRevB.94.165301.
- (36) Molas, M. R.; Faugeras, C.; Slobodeniuk, A. O.; Nogajewski, K.; Bartos, M.; Basko, D. M.; Potemski, M. Brightening of Dark Excitons in Monolayers of Semiconducting Transition Metal Dichalcogenides. *2D Mater.* **2017**, *4* (2), 021003. https://doi.org/10.1088/2053-1583/aa5521.
- (37) Selig, M.; Berghäuser, G.; Richter, M.; Bratschitsch, R.; Knorr, A.; Malic, E. Dark and Bright Exciton Formation, Thermalization, and Photoluminescence in Monolayer Transition Metal Dichalcogenides. *2D Mater.* **2018**, *5* (3), 035017. https://doi.org/10.1088/2053-1583/aabea3.

- (38) Frisenda, R.; Drüppel, M.; Schmidt, R.; Michaelis de Vasconcellos, S.; Perez de Lara, D.; Bratschitsch, R.; Rohlfing, M.; Castellanos-Gomez, A. Biaxial Strain Tuning of the Optical Properties of Single-Layer Transition Metal Dichalcogenides. *npj 2D Mater Appl* **2017**, *1* (1), 10. https://doi.org/10.1038/s41699-017-0013-7.
- (39) Desai, S. B.; Madhvapathy, S. R.; Amani, M.; Kiriya, D.; Hettick, M.; Tosun, M.; Zhou, Y.; Dubey, M.; Ager III, J. W.; Chrzan, D.; Javey, A. Gold-Mediated Exfoliation of Ultralarge Optoelectronically-Perfect Monolayers. *Advanced Materials* **2016**, *28* (21), 4053–4058. https://doi.org/10.1002/adma.201506171.
- (40) Kresse, G. G. Kresse and J. Furthmüller, Phys. Rev. B 54, 11169 (1996). *Phys. Rev. B* 1996, 54, 11169.
- (41) Perdew, J. P. JP Perdew, A. Ruzsinszky, GI Csonka, OA Vydrov, GE Scuseria, LA Constantin, X. Zhou, and K. Burke, Phys. Rev. Lett. 100, 136406 (2008). *Phys. Rev. Lett.* **2008**, *100*, 136406.
- (42) Perdew, J. P. JP Perdew, K. Burke, and M. Ernzerhof, Phys. Rev. Lett. 77, 3865 (1996). *Phys. Rev. Lett.* **1996**, 77, 3865.
- (43) Wang, V.; Xu, N.; Liu, J.-C.; Tang, G.; Geng, W.-T. VASPKIT: A User-Friendly Interface Facilitating High-Throughput Computing and Analysis Using VASP Code. *Computer Physics Communications* **2021**, *267*, 108033.